Effect of Positron Range on PET Quantification in Diseased and Normal Lungs

Elise C. Emond[1], Ashley M. Groves[1], Brian F. Hutton[1,2], Kris Thielemans[1]

[1] Institute of Nuclear Medicine, University College London, London NW1 2BU, UK.
[2] Centre for Medical Radiation Physics, University of Wollongong, Wollongong NSW 2522, Australia.

E-mail: elise.emond.16@ucl.ac.uk

Abstract. The impact of positron range on PET image reconstruction has often been investigated as a blurring effect that can be partly corrected by adding an element to the PET system matrix in the reconstruction, usually based on a Gaussian kernel constructed from the attenuation values. However, the physics involved in PET is more complex. In regions where density does not vary, positron range indeed involves mainly blurring. However, in more heterogeneous media it can cause other effects. This work focuses on positron range in the lungs and its impact on quantification, especially in the case of pathologies such as cancer or pulmonary fibrosis, for which the lungs have localised varying density. Using Monte Carlo simulations, we evaluate the effects of positron range for multiple radionuclides (^{18}F, ^{15}O, ^{68}Ga, ^{89}Zr, ^{82}Rb, ^{64}Cu and ^{124}I) as, for novel radiotracers, the choice of the labelling radionuclide is important. The results demonstrate quantification biases in highly heterogeneous media, where the measured uptake of high-density regions can be increased by the neighbouring radioactivity from regions of lower density, with the effect more noticeable for radionuclides with high-energy positron emission. When the low-density regions are considered to have less radioactive uptake (e.g. due to the presence of air), the effect is less severe.

1. Introduction

Positron Emission Tomography (PET) is a nuclear imaging technique that allows imaging of metabolic processes of tissues or organs, providing "functional" information that can be quantified. Resolution in PET is poorer than in many other imaging modalities, such as Computerised Tomography (CT) or Magnetic Resonance Imaging (MRI). Some of the resolution degrading factors in PET are linked to the scanner specifications while others are directly linked to the physical interactions involved. In PET, a radiotracer – a biological molecule labelled with a positron-emitting radionuclide – is given to the patient. Through collisions with several bound electrons of the medium, the kinetic energy of one emitted positron decreases and, eventually, it annihilates with an electron; this interaction results usually in the creation of 2 γ photons of 511 keV that travel almost back-to-back to opposite detectors of the PET scanner (Evans 1955). The

PET images are then produced via coincidence detection of these two photons. Hence, in normal practice the reconstructed PET image does not directly describe the distribution of radioactivity, but the distribution of the annihilation events. The distance between the location of the emission of the positron and its annihilation with an electron is known as "positron range" (Lehnert et al. 2011, Derenzo 1979). Since the probability of annihilation increases as the kinetic energy of the positron decreases due to collisions with electrons, the positron range depends on the initial kinetic energy of the positron at emission and the density and composition of the media crossed by the positron before it annihilates. Its effect on the overall resolution is small for ^{18}F, the clinically most commonly used radionuclide. However, the resolution degradation linked to positron range is greater for radionuclides emitting higher energy positrons and in tissues of low density, such as the lung. Estimated values will be given for some common radionuclides in Table 2.

Whereas the density of healthy lungs is relatively uniform (aside from airways and blood vessels), some pathologies can affect the local structure and density of the lung, for example in the case of lung cancer or interstitial lung diseases. In these cases, the effect of positron range is spatially variant, and image quantification can be impacted. In order to establish whether a local apparent increase in radioactivity corresponds to a specific tracer uptake, the effect must be studied carefully.

From a physics perspective, the lung consists predominantly of three types of materials; for normal lung, the average fractions have been estimated as follows: 74% air, 16% blood and 10% "lung cells" (i.e. everything in the lung except air and blood) (Chen et al. 2017). However, pulmonary pathologies can lead to a local or global change of the lung architecture, including for example a localised decrease of the air content, that can affect the quantification of PET images. In this paper we will refer to lung "tissue" as being everything in the lung except the air, similarly as in Lambrou et al. (2011).

Lung cancer is one of the main causes of death in the world and the main cause of cancer mortality worldwide (Postmus et al. 2017). Tumour staging and follow-up are essential for a better prognosis, with increased utilisation of PET/CT imaging, particularly via measurement of ^{18}F-FDG uptake (Nakamura et al. 2015). Most lung tumours have a density close to that of soft tissue ($\approx 1\,\mathrm{g\cdot cm^{-3}}$, Xu et al. (2008)), whereas the rest of the lung has a far lower density ($\approx 0.26\,\mathrm{g\cdot cm^{-3}}$). This means that there is usually an abrupt change of density at the interface of the tumour with the rest of the lung. In the case of idiopathic pulmonary fibrosis (IPF) – characterised by a build-up of scarring tissue within the lungs – the fibrotic regions of the lungs have an increased density compared to the healthy parts of the lungs. Localised high-density structures, such as honeycombing, increase in extent as disease progresses (Spagnolo et al. 2015).

Several radionuclides will be studied in this work: ^{18}F, ^{68}Ga, ^{82}Rb, ^{15}O, ^{89}Zr, ^{64}Cu and ^{124}I. Besides ^{18}F, ^{68}Ga is increasingly used to label biological ligands such as DOTATATE which targets somatostatin receptors. Another example is prostate-specific membrane antigen (^{68}Ga-PSMA) which targets tumour neovasculature and has shown

promising results, mainly for prostate cancer but also more recently in the lung (Chang et al. 1999, Wang et al. 2015). ^{68}Ga has the disadvantage of having a larger positron range than ^{18}F. ^{82}Rb or ^{15}O are less commonly used in PET lung imaging, however these can be used to evaluate perfusion. Other radionuclides of recent interest in PET are ^{89}Zr, ^{64}Cu and ^{124}I which, because of their relatively long half-life, are potentially useful for imaging lung cancers using radiolabelled monoclonal antibodies, for which the circulation half-life is generally on the order of days (Reichert & Valge-Archer 2007).

In the case of a positron-emitting point source, the probability of annihilation can be expressed as a 3D distribution and the image corresponding to the annihilation events ("annihilation image") can be viewed as the convolution by a blurring kernel of the image corresponding to the positron emission events ("emission image"). In uniform media, previous work on estimating positron range involved computation of 1D or 2D annihilation range distributions from the actual distribution (Blanco 2006, Levin & Hoffman 1970, Derenzo 1979, Cal-González et al. 2010, Jødal et al. 2012, Cal-González et al. 2013). Although using one of the previous methods is satisfactory in a relatively uniform medium, it may be inaccurate in highly heterogeneous media or near a boundary between two regions with very different densities. In fact, a noticeable difference compared to a homogeneous medium is that the centre of gravity for activity is not located at the emission source point, i.e. a shift occurs. We illustrate this here with a boundary between a high-density medium and a low-density medium (tumour and healthy lung), obtained from a GATE (Jan et al. 2004) Monte Carlo simulation (see later in this paper for more details), in Figure 1. In non-homogeneous tissue, the positron range can be modelled using spatially-variant anisotropic kernels. A good model should take into account the difference of densities in a neighbourhood. Several strategies already exist (Bai et al. 2003, Szirmay-Kalos et al. 2012, Alessio & MacDonald 2008, Cal-González et al. 2015), but have not been validated in humans and may not be applicable to heterogeneous lungs or for all radionuclides. Furthermore it might be impractical in clinical settings due to rather lengthy processing. Another possibility for non-homogeneous media is to use Monte Carlo simulations (Lehnert et al. 2011) to obtain the positron range distribution via simulations of all possible physical interactions given a radioactivity distribution. The latter are also computationally expensive and unsuitable for routine use, but represent a gold standard to assess the effect of positron range on PET images.

This paper is organised as follows. We briefly discuss the effect of positron range in uniform media, then describe the Monte Carlo methodology of this paper in detail. Last, we present results of the effect of positron range in the lungs, in the presence of small high-density structures within the healthy lung, such as tumour, localised fibrosis or blood vessels.

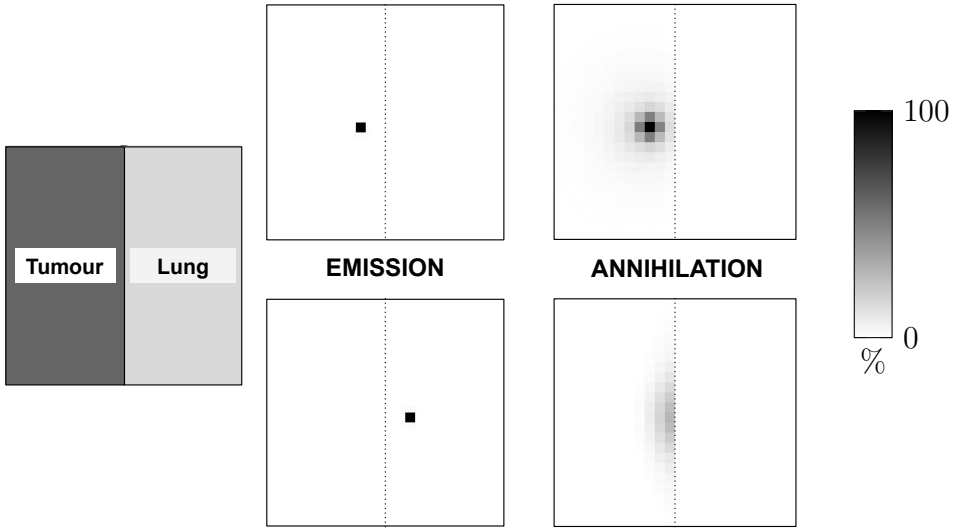

Figure 1: Illustration of positron range effect for a radioactive ^{82}Rb emission source placed in close proximity (6 mm) to an abrupt density change, showing the number of emission and annihilation events - emission either in the tumour (top) or in the (healthy) lung (bottom). The annihilation images (image size of $7.2 \times 7.2 \times 7.2\,\mathrm{cm}^3$ with voxel of size: $3 \times 3 \times 3\,\mathrm{mm}^3$) were scaled to 1% of the total number of emitted positrons ($\approx 918,000$ for both simulations).

2. Theory and Methodology

2.1. Monte Carlo Simulation Settings

In this work, we used GATE (version 8.2), Monte Carlo simulation software dedicated to medical imaging (Jan et al. 2004), to simulate the effect of positron range in the lung. GATE is based on the GEANT4 toolkit (version 10.5.1), which simulates the particle behaviour through physical matter (Agostinelli et al. 2003); the GATE physics list "*empenelope*" accounts for most of the physical interactions involved in PET imaging to obtain an accurate model of the path an emitted positron takes before annihilating with an electron, including multiple scattering, ionisation, annihilation or production of bremsstrahlung. The energy distribution function, for a single β^+ transition, can be approximated as (Levin & Hoffman 1970):

$$N(E)\,\mathrm{d}E = p\,F(Z-1,E)\left(1+\frac{E}{0.511}\right)(E_{\max}-E)^2\,\mathrm{d}E \tag{1}$$

where:

- Z is the atomic number of the mother nucleus, prior beta decay.
- E is the kinetic energy of the positron in MeV.
- $E_{\max}$ is the maximum kinetic energy for the radionuclide, in MeV.

Table 1: Maximum kinetic energy and atomic number of the studied PET radionuclides (Laboratoire National Henri Becquerel 2018, Brookhaven National Laboratory 2019)

Radionuclide	$E_{\max}$	Z
^{18}F	0.635	9
^{64}Cu	0.653	29
^{89}Zr	0.902	40
^{15}O	1.723	8
^{68}Ga	1.899	31
^{124}I (1)	1.535	53
^{124}I (2)	2.138	53
^{82}Rb (1)	2.605	37
^{82}Rb (2)	3.381	37

- $p = \sqrt{\left(1 + \frac{E}{0.511}\right)^2 - 1}$ is the momentum of the positron.
- $F(Z, E) = \frac{2\pi\eta}{1-e^{-2\pi\eta}}$ is the Fermi function, where:
  - $\eta = -\frac{Z\alpha}{p} \times (1 + \frac{E}{0.511})$, for positron decay.
  - $\alpha \approx 1/137$ the fine-structure constant, used in fundamental physics.

Mathematica (Wolfram Research 2017) was used to obtain histograms corresponding to the energy distribution of the studied radionuclides, using the values of Z and $E_{\max}$ in Table 1. Whereas the decay schemes of ^{18}F, ^{15}O, ^{68}Ga, ^{89}Zr, ^{64}Cu are simple (only one β^+ transition), ^{82}Rb and ^{124}I have several β^+ transitions. For both radionuclides, the previous formula 1 was applied to the two transitions with the highest probabilities to create a total energy distribution as a weighted sum of the separate energy spectra. The resulting energy spectra are shown in Figure 2. The histogrammed spectra were incorporated in GATE as user-defined spectra.

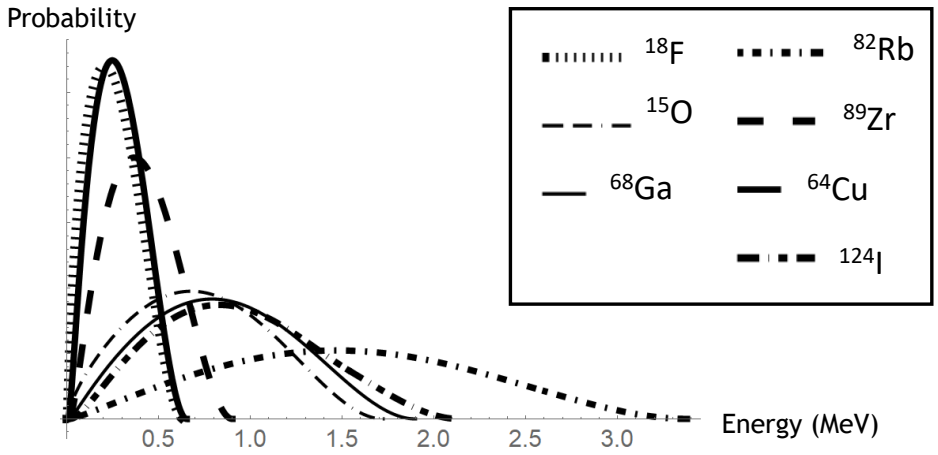

Figure 2: Positron emission energy spectra for the different radioisotopes of this study

Simple point source simulations in water were performed to assess the validity of the settings by calculating the mean and maximal positron ranges (R_{mean} and R_{max} respectively) from the GATE output, see Table 2. The values were in good agreement with Lehnert et al. (2011) for both ^{18}F and ^{15}O, as well as with other more sophisticated positron range models, although slightly lower.

Table 2: Positron ranges estimated and in literature, in water for the studied radionuclides.

	Estimated		Literature	
Radionuclide	R_{mean} (mm)	R_{max} (mm)	R_{mean} (mm)	R_{max} (mm)
^{18}F	0.44	2.31	0.48[a],0.57[b],0.6[c]	2.27[a],1.85[b],2.6[c]
^{64}Cu	0.51	2.54	0.56[d]	2.9[d]
^{89}Zr	0.87	3.76	1.27[d]	4.2[d]
^{15}O	2.00	8.01	2.21[a],2.34[b],2.5[c]	7.96[a],7.70[b],9.1[c]
^{68}Ga	2.39	9.57	2.69[b],2.9[c]	8.86[b],10.3[c]
^{124}I	2.70	10.57	3.4[d]	11.7[d]
^{82}Rb	5.03	16.80	5.33[b],5.9[c]	17.6[b],18.6[c]

a: Lehnert et al. (2011), b: Cal-González et al. (2010), c: Jødal et al. (2012), d: Jødal et al. (2014)

In addition to the definition of radioactive sources, "materials" need to be defined in GATE to create the simulation phantom. These are defined by the physical elements comprising them, their fractions, as well as their corresponding mass density. The default GATE material database comprises only one "Lung" material, which corresponds to the average composition and density of 'normal' lung. A material corresponding to a malignant lung tumour was added to the database with an average CT value of 11 ($\approx 1.028\,\text{g}\cdot\text{cm}^{-3}$, Xu et al. (2008)) (see Appendix A). In the case of the fibrotic lung, as its composition is spatially variant depending on the degree of fibrosis, the material database was modified to incorporate a range of fibrotic lung materials, that correspond to lung tissues between -800 HU ($\approx 0.26\,\text{g}\cdot\text{cm}^{-3}$, healthy lung) to -200 HU ($\approx 0.615\,\text{g}\cdot\text{cm}^{-3}$, severely fibrotic lung), with a step of 50 HU ($\approx 0.3\,\text{g}\cdot\text{cm}^{-3}$), using the different lung fractions given in Chen et al. (2017). The details of the fibrotic lung materials are given in Appendix B.

2.2. Additional Factors Affecting Resolution in PET

Aside from positron range, PET resolution also depends on other factors such as detection uncertainties, acolinearity or the reconstruction method (Moses 2011). The typical spatial resolution for a clinical scanner, characterised for a very small object source in air comparable to a point source (negligible positron range effect), is approximately 5 mm (Bettinardi et al. 2011, Jakoby et al. 2011, Kolthammer et al. 2015). In addition, postfiltering is generally used in PET reconstruction. In clinical practice, a Gaussian postfilter of Full-Width at Half Maximum (FWHM) $\approx$ 6 mm is typically

applied, resulting in a global spatial blurring that we can model via a normal distribution of FWHM equal to $\sqrt{5^2+6^2} \approx 8\,\text{mm}$. In the following simulations, the raw results will be either filtered via a Gaussian filter of FWHM 5 mm or 8 mm to be able to study the effect of positron range on quantification of reconstructed images in more realistic conditions.

2.3. Simulation Processing

From the output from a GATE Monte Carlo simulation, the locations of all positron emission events and the locations of all annihilation events were recorded.

The emission events corresponding to annihilations occurring outside of the phantom were discarded. In our simulations, the "emission image" $\boldsymbol{E}$ and "annihilation image" $\boldsymbol{A}$ are computed. These two images were either used directly or postfiltered in order to mimic measures on PET reconstructed images (see Section 2.2), using two different Gaussian filters FWHM: 5 mm (unfiltered reconstructed images) and 8 mm (filtered reconstructed images). From these images, the "apparent recovery ratio" α of a volume-of-interest (VOI) can be computed, measuring the increase or decrease in activity within the volume due solely to positron range and postfiltering (if any). In a VOI $\mathcal{V}$, we denote:

$$\alpha_{\mathcal{V},i} = \frac{A_{\mathcal{V},i}}{E_{\mathcal{V},i}} \tag{2}$$

where $A_{\mathcal{V},i}$ (respectively $E_{\mathcal{V},i}$) is the mean number of events in the annihilation image (respectively the emission image) within $\mathcal{V}$, after postfiltering with a Gaussian of FWHM i mm. In addition to the apparent recovery ratio, the "apparent contrast" $\mathcal{C}_{\mathcal{V}_1/\mathcal{V}_2,i}$, defined as the ratio of $A_{\mathcal{V}_1,i}$ and $A_{\mathcal{V}_2,i}$ is calculated to compare the uptake of a VOI $\mathcal{V}_1$ to that of a VOI $\mathcal{V}_2$, after a postfilter of FWHM i mm was applied on the images.

The same definitions are extended to ensembles of VOIs $\{\mathcal{V}_k\}_{k\in\mathbb{N}}$ and $\{\mathcal{W}_k\}_{k\in\mathbb{N}}$, where $\alpha_{\mathcal{V},i} = \overline{\alpha_{\mathcal{V}_k,i}}$ and $\mathcal{C}_{\mathcal{V}/\mathcal{W},i} = \sum_k \alpha_{\mathcal{V}_k,i} \Big/ \sum_k \alpha_{\mathcal{W}_k,i}$, in which $\overline{\cdot}$ represents the "mean" operator.

When comparing the effect of positron range between two complementary media (i.e. there are only two types of material in the simulation and all events are emitted and annihilated in either of those), we also compute the fraction $\mathcal{S}_{\mathcal{R}_1/\mathcal{R}_2}$ of the number of emission events emitted from one medium $\mathcal{R}_2$ but annihilated in the other medium $\mathcal{R}_1$ over the number of emission events emitted from $\mathcal{R}_1$ but annihilated in $\mathcal{R}_2$. This measure will be described as the "spillover" ratio of $\mathcal{R}_1$ in $\mathcal{R}_2$. If the ratio is > 1 (resp. < 1), this means that the apparent uptake of the entire $\mathcal{R}_1$ is overestimated (resp. underestimated) because of positron range effects.

3. Simulations

Two pulmonary pathologies were considered in this work, for which two different radioactivity distributions were simulated. The different phantoms and scenarios are

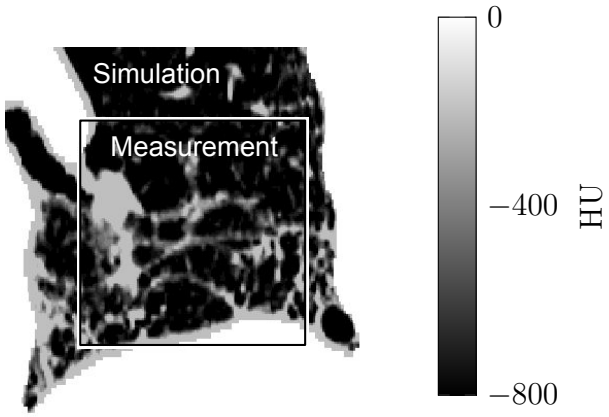

Figure 3: Coronal view of the density image used in the simulation showing the simulation volume (all image) and measurement volume (within the box).

presented in this section.

3.1. Simulations of a Spherical Lung Tumour of Variable Radius

Spherical tumours with three different diameters (1 cm, 2 cm and 3 cm) were simulated in the normal lung. The VOIs corresponding to the tumours are denoted as $\mathcal{T}_1$, $\mathcal{T}_2$ and $\mathcal{T}_3$ (corresponding to diameters of 1 cm, 2 cm and 3 cm, respectively). The images of annihilation and emission were computed using voxels of dimension $1 \times 1 \times 1\,\mathrm{mm}^3$.

3.2. Simulations of a Fibrotic Lung

A diagnostic CT image volume from an IPF patient was used to perform a realistic simulation of a fibrotic lung. The latter was obtained from a GE Discovery 690, multislice helical CT acquisition at breathhold covering 27.5 cm with a 1.25 mm slice thickness and a pitch of 0.516, with 120 kVp, 149 mA and 0.6 s revolution time. The image was segmented into several fibrotic lung materials, according to their Hounsfield value (Section 2.1). The outside of the lung was considered as liquid water for the simulation (GATE default database: $d = 1\,\mathrm{g \cdot cm^{-3}}$). For computational reasons, the original CT image was cropped to a volume of $10 \times 10 \times 10\,\mathrm{cm}^3$ for the simulation. In order to avoid issues with border effects, the emission and annihilation events occurring near the edges of the input CT image were not considered and the measurements were made within a volume of $6 \times 6 \times 6\,\mathrm{cm}^3$. A slice through the CT image is presented in Figure 3.

The images of annihilation and emission were computed using voxels of dimension $0.5 \times 0.5 \times 0.5\,\mathrm{mm}^3$ and were analysed using two VOI sizes - small ($3 \times 3 \times 3\,\mathrm{mm}^3$) and medium-sized ($9 \times 9 \times 9\,\mathrm{mm}^3$) – at 20 locations – determined on the density map:

* 10 predominantly normal lung
  - small VOIs "$\mathcal{N}_1$": mean density ± standard deviation = $0.263 \pm 0.016\,\mathrm{g \cdot cm^{-3}}$

  - medium-sized VOIs "$\mathcal{N}_2$": mean density ± standard deviation = $0.274 \pm 0.045\,\mathrm{g \cdot cm^{-3}}$

* 10 predominantly fibrotic lung
  - small VOIs "$\mathcal{F}_1$": mean density ± standard deviation = $0.574 \pm 0.171\,\mathrm{g \cdot cm^{-3}}$
  - medium-sized VOIs "$\mathcal{F}_2$": mean density ± standard deviation = $0.431 \pm 0.224\,\mathrm{g \cdot cm^{-3}}$

3.3. Radioactivity Distributions

For each simulation presented above, two radioactivity distributions were assessed:

- *Scenario 1*: the radioactivity concentration is uniform throughout the whole lung.
- *Scenario 2*: the radioactivity concentration is uniform in the "tissue" (introduced previously in 1 as everything in the lung outside the air) and that there is no radioactivity in the air. The resulting radioactivity concentration in each voxel is therefore obtained by multiplying with $1 - V_a$, where V_a is the air fraction in the lung medium (given in Appendix B).

The minimal numbers of emission/annihilation events retained are the following: (1) Lung Tumours: $\approx 2 \cdot 10^8$ for Scenario 1 and $\approx 5 \cdot 10^7$ for Scenario 2, (2) Fibrotic Lung: $\approx 8 \cdot 10^7$ for Scenario 1 and $\approx 3 \cdot 10^7$ for Scenario 2. In both scenarios, the neighbouring soft tissue does not have any radioactivity. For conciseness, only images corresponding to the simulations of ^{18}F, ^{68}Ga and ^{82}Rb will be shown in this publication. Note that ^{89}Zr and ^{64}Cu have similar energy spectra to ^{18}F and ^{15}O and ^{124}I to ^{68}Ga 2, therefore similar positron ranges.

In the case of the lung tumour simulations, in order to study the effect of the "background" level (i.e., the relative amount of activity in the healthy lung respectively to the tumour), intermediary apparent recovery values were found from the results of Scenario 1, by rescaling the annihilation and emission images corresponding to emission events occurring in the healthy tissue.

4. Results

4.1. Simulation of Spherical Lung Tumours

4.1.1. Scenario 1: The apparent recovery α measured from the different tumours $\mathcal{T}_1$, $\mathcal{T}_2$ and $\mathcal{T}_3$ for scenario 1 can be found in Table 3, including measures made before and after postfiltering.

Before any postfiltering, a halo can be seen on the outside edge of the tumour, see images corresponding to $\mathcal{T}_2$ in Figure 4. After postfiltering, the halo either almost disappears (^{18}F, ^{89}Zr and ^{64}Cu) or is blurred out to appear as an increased uptake in the tumour compared to the healthy lung background (^{82}Rb, ^{124}I, ^{68}Ga and ^{15}O). The effect is amplified for ^{82}Rb where the tumour resembles a hot spot on the image.

Table 3: Lung Tumour - Scenario 1 - Apparent recovery computed from the emission and annihilation images for the studied radionuclides in the tumour (diameters: 1 cm, 2 cm and 3 cm). $\alpha_{\mathcal{T}_k,i}$ is the apparent recovery for a tumour of diameter k cm, after a postfilter of FWHM i mm.

Radionuclide	$\alpha_{\mathcal{T}_1,0}$	$\alpha_{\mathcal{T}_1,5}$	$\alpha_{\mathcal{T}_1,8}$	$\alpha_{\mathcal{T}_2,0}$	$\alpha_{\mathcal{T}_2,5}$	$\alpha_{\mathcal{T}_2,8}$	$\alpha_{\mathcal{T}_3,0}$	$\alpha_{\mathcal{T}_3,5}$	$\alpha_{\mathcal{T}_3,8}$
^{18}F	1.116	1.029	1.011	1.060	1.018	1.010	1.040	1.013	1.007
^{64}Cu	1.146	1.041	1.017	1.073	1.024	1.014	1.049	1.017	1.010
^{89}Zr	1.292	1.097	1.042	1.147	1.059	1.036	1.098	1.041	1.027
^{15}O	1.766	1.348	1.179	1.403	1.224	1.157	1.269	1.156	1.115
^{68}Ga	1.918	1.434	1.229	1.490	1.284	1.203	1.329	1.199	1.149
^{124}I	2.072	1.525	1.284	1.497	1.290	1.209	1.379	1.237	1.182
^{82}Rb	2.705	1.915	1.513	2.038	1.717	1.550	1.718	1.520	1.421

Table 4: Lung Tumours - Scenario 1 - Spillover ratios corresponding to the tumour, computed from the emission and annihilation images for the studied radionuclides in the tumour (diameters: 1 cm, 2 cm and 3 cm). $\mathcal{T}_k$ represents the tumour of diameter k cm.

Radionuclide	$\mathcal{S}_{\mathcal{T}_1/\mathcal{N}}$	$\mathcal{S}_{\mathcal{T}_2/\mathcal{N}}$	$\mathcal{S}_{\mathcal{T}_3/\mathcal{N}}$
^{18}F	1.987	1.680	1.840
^{64}Cu	2.111	1.801	1.941
^{89}Zr	2.498	2.239	2.351
^{15}O	3.102	2.977	3.046
^{68}Ga	3.198	3.087	3.161
^{124}I	3.344	3.116	3.247
^{82}Rb	3.482	3.442	3.494

The spillover ratios for the tumours $\mathcal{T}_1$, $\mathcal{T}_2$ and $\mathcal{T}_3$ in the background $\mathcal{N}$ are given in Table 4, where $\mathcal{N}$ represents the outside of the tumour, comprising normal lung.

All measures show that the shift of radioactivity from the outside of the tumours, that is low-density lung, to the tumour is greater than the opposite, i.e. the shift from the tumour to the normal lung.

4.1.2. Scenario 2: The recovery ratios were all close to 1 (with and without postfiltering), see in Table 5. The images for $\mathcal{T}_2$ are shown in Figure 5.

Visually the images for ^{18}F, ^{68}Ga and ^{82}Rb are almost identical. However, the measured values show that the effect observed in Scenario 2 is dominated by the "spill-out", i.e. there are more positrons emitted from the tumours that are annihilated in the normal lung than the opposite. This can be verified by computing, on the unfiltered images, the spillover ratios of the tumours. The results are given in Table 6 for all radionuclides (where $\mathcal{N}$ represents the outside of the tumour, comprising normal lung).

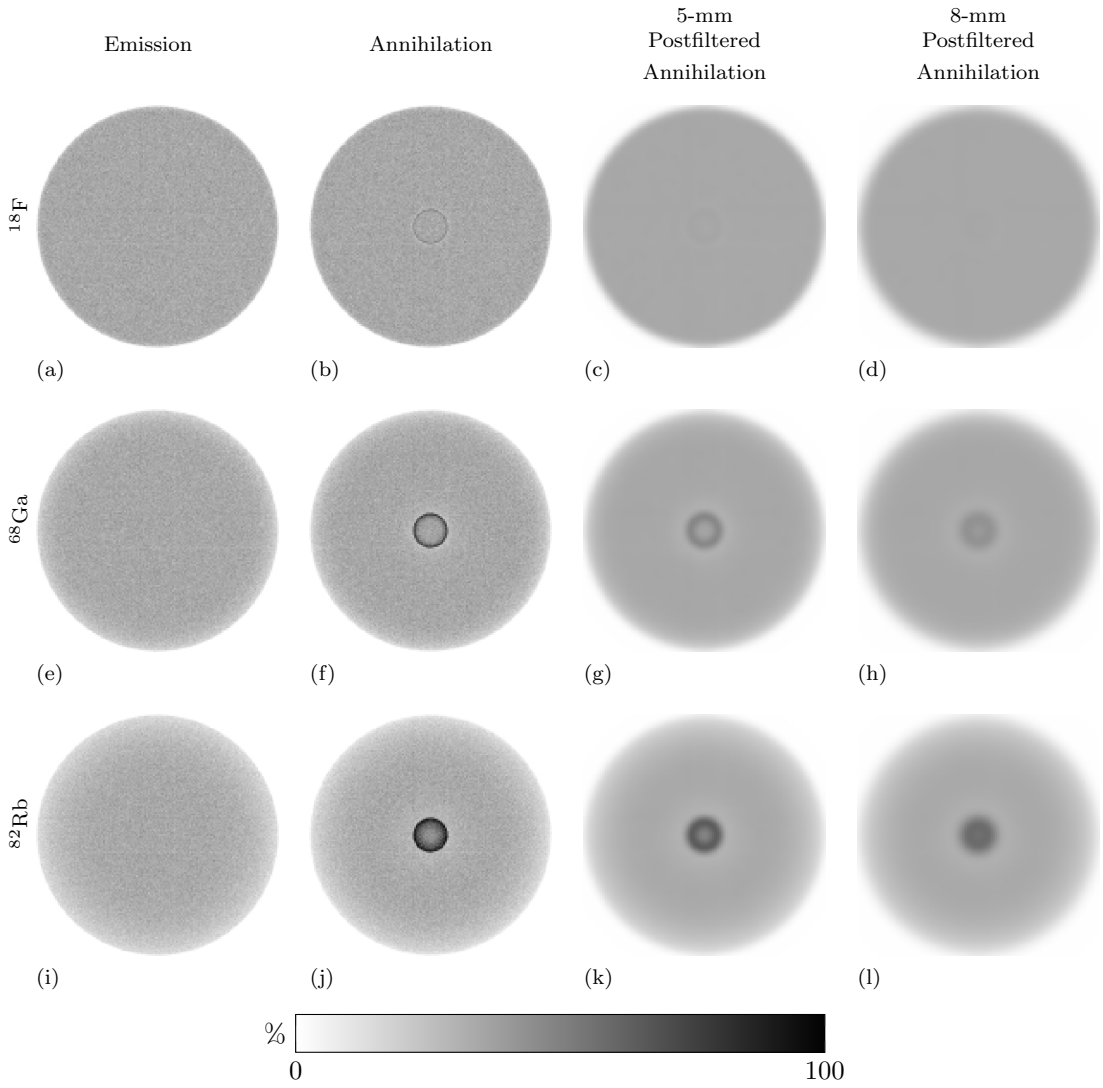

Figure 4: Lung Tumour (2 cm) - Scenario 1 - (a) (resp. (e), (i)) emission events, (b) (resp. (f), (j)) annihilation events, (c) (resp. (g), (k)) 5 mm postfiltered annihilation events and (d) (resp. (h), (l)) 8 mm postfiltered annihilation events computed for ^{18}F (top row) (resp. ^{68}Ga (middle row), ^{82}Rb (bottom row)). All images are scaled using the same colourbar (maximal value of the unfiltered ^{82}Rb annihilation image).

The spillover ratios are indeed all inferior to 1.

4.1.3. Intermediary Scenarios The change of balance between spill-in and spill-out can be observed in Figure 6 (for ^{18}F, ^{68}Ga and ^{82}Rb and tumours of 1 cm and 2 cm). The plots show the apparent recovery values for different levels of activity in the healthy lung ("background") after a 8-mm postfilering. For this type of small tumours, it appears that the apparent recovery are ≈ 1 when $\lambda_{\mathcal{T}}/d_{\mathcal{T}} \approx \lambda_{\mathcal{N}}/d_{\mathcal{N}}$ (where $\lambda_{\mathcal{T}}$ (resp. $\lambda_{\mathcal{N}}$) is the activity concentration in the tumour (resp. the healthy lung) and $d_{\mathcal{T}}$ (resp. $d_{\mathcal{N}}$) is

Table 5: Lung Tumours - Scenario 2 - Apparent recovery computed from the emission and annihilation images for the studied radionuclides in the tumour (diameters: 1 cm, 2 cm and 3 cm). $\alpha_{\mathcal{T}_k,i}$ is the apparent recovery for a tumour of diameter k cm, after a postfilter of FWHM i mm.

Radionuclide	$\alpha_{\mathcal{T}_1,0}$	$\alpha_{\mathcal{T}_1,5}$	$\alpha_{\mathcal{T}_1,8}$	$\alpha_{\mathcal{T}_2,0}$	$\alpha_{\mathcal{T}_2,5}$	$\alpha_{\mathcal{T}_2,8}$	$\alpha_{\mathcal{T}_3,0}$	$\alpha_{\mathcal{T}_3,5}$	$\alpha_{\mathcal{T}_3,8}$
^{18}F	1.002	0.998	0.997	1.001	1.000	0.999	1.001	1.000	1.000
^{64}Cu	1.002	0.999	0.998	1.001	1.000	0.999	1.001	1.000	1.000
^{89}Zr	1.006	0.999	0.996	1.003	1.000	0.999	1.001	1.000	1.000
^{15}O	1.004	0.997	0.990	1.005	1.003	1.001	1.003	1.002	1.001
^{68}Ga	1.011	1.003	0.993	1.004	1.002	1.000	1.003	1.002	1.001
^{124}I	1.017	1.009	0.999	1.006	1.004	1.002	1.004	1.003	1.002
^{82}Rb	1.013	1.006	0.995	1.006	1.005	1.010	1.004	1.004	1.003

Table 6: Lung Tumours - Scenario 2 - Spillover ratios corresponding to the tumour, computed from the emission and annihilation images for the studied radionuclides in the tumour (diameters: 1 cm, 2 cm and 3 cm). $\mathcal{T}_k$ represents the tumour of diameter k cm.

Radionuclide	$\mathcal{S}_{\mathcal{T}_1/\mathcal{N}}$	$\mathcal{S}_{\mathcal{T}_2/\mathcal{N}}$	$\mathcal{S}_{\mathcal{T}_3/\mathcal{N}}$
^{18}F	0.523	0.441	0.480
^{64}Cu	0.556	0.469	0.504
^{89}Zr	0.660	0.588	0.612
^{15}O	0.800	0.775	0.793
^{68}Ga	0.843	0.805	0.821
^{124}I	0.865	0.827	0.844
^{82}Rb	0.904	0.897	0.911

the mass density of the tumour (resp. the healthy lung)), i.e., which is equivalent to Scenario 2. Below that threshold (indicated by the vertical dotted line in Figure 6) the change in spill-in/spill-out fractions leads to a negative bias in the apparent recovery of the tumour. This is also the case for other radionuclides and tumour of 3 cm.

4.2. Simulation of a Fibrotic Lung

4.2.1. Scenario 1: The emission images and the unfiltered and filtered annihilation images for the seven studied radionuclides can be found in Figure 7, with the corresponding measures of apparent recovery and apparent contrast for different postfiltering in Tables 7 and 8.

This case is similar to Scenario 1 of the tumour simulations: when the radioactivity is evenly distributed among the different lung types, the fibrotic parts of the lung (corresponding to the regions with higher density) appear to have higher radioactivity concentration than the normal lung.

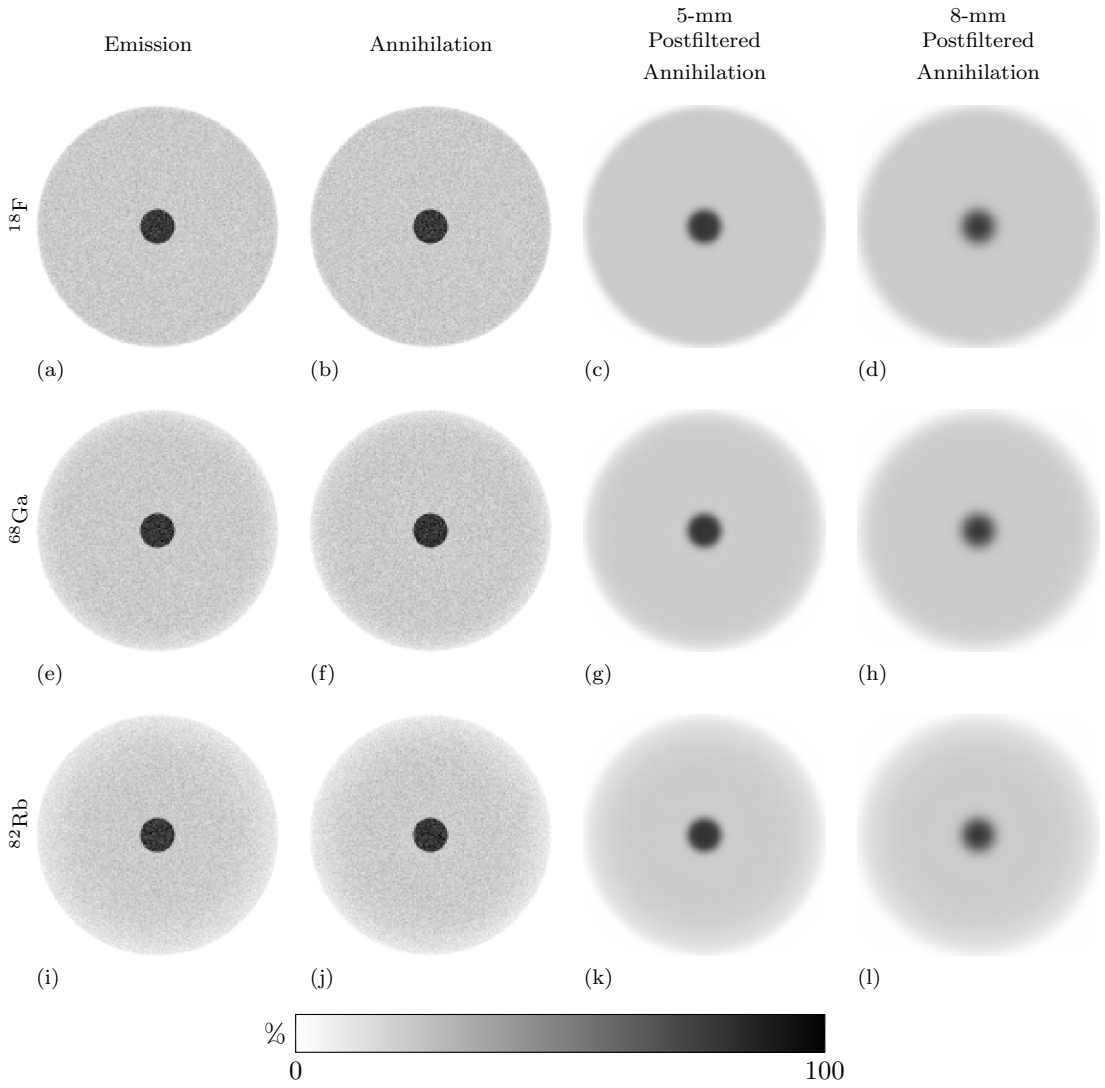

Figure 5: Lung Tumour (2 cm) - Scenario 2 - (a) (resp. (e), (i)) emission events, (b) (resp. (f), (j)) annihilation events, (c) (resp. (g), (k)) 5 mm postfiltered annihilation events and (d) (resp. (h), (l)) 8 mm postfiltered annihilation events computed for ^{18}F (top row) (resp. ^{68}Ga (middle row), ^{82}Rb (bottom row)). All images are scaled using the same colourbar (maximal value of the unfiltered ^{82}Rb annihilation image).

4.2.2. Scenario 2: The emission images and the unfiltered and filtered annihilation images for the seven studied radionuclides can be found in Figure 8, with the corresponding measures of apparent recovery values for different amounts of postfiltering in Table 9. Similarly as Scenario 2 for the tumours, especially ^{82}Rb, the apparent recovery ratio values do not demonstrate a positive quantitative bias in the high-density medium (here the fibrosis) due to positron range, but a negative bias; this suggests that more positrons emitted from the fibrotic lung are annihilated in the normal lung than the opposite.

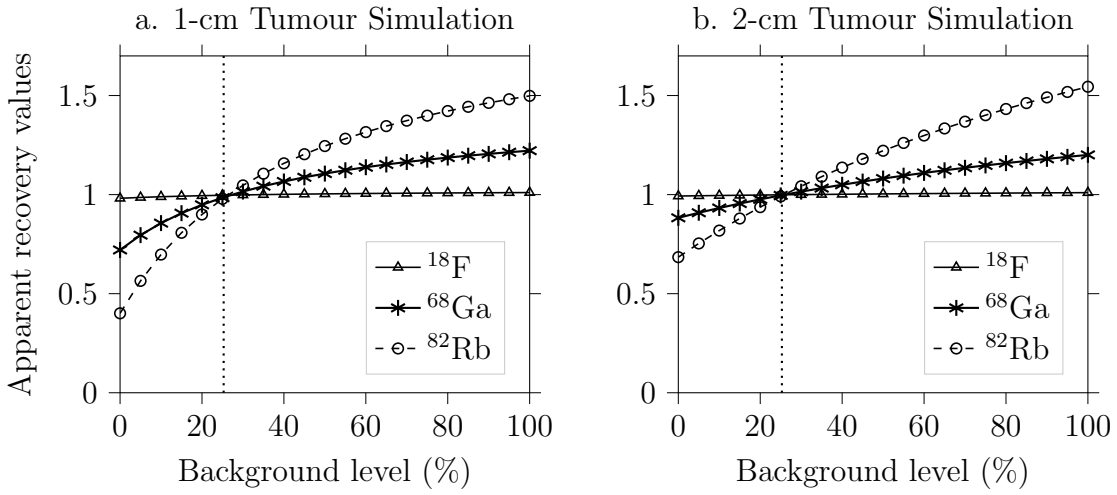

Figure 6: Plots showing the apparent recovery values (a.) $\alpha_{\mathcal{T}_1,8}$ (tumour of diameter 1 cm) and (b.) $\alpha_{\mathcal{T}_2,8}$ (tumour of diameter 2 cm), for different background levels (8-mm Gaussian postfiltering). The vertical dotted line indicates the threshold value for which the apparent recovery values are ≈ 1 for all radionuclides.

Table 7: Fibrotic Lung - Scenario 1 - Mean apparent recovery values computed from the original emission and annihilation images for all studied radionuclides. $\alpha_{\mathcal{V},i}$ is the apparent recovery for a VOI $\mathcal{V}$ (description in 3.2), after a postfilter of FWHM i mm.

Measure	^{18}F	^{64}Cu	^{89}Zr	^{15}O	^{68}Ga	^{124}I	^{82}Rb
$\alpha_{\mathcal{N}_1,0}$	0.987	0.970	0.976	0.924	0.918	0.896	0.820
$\alpha_{\mathcal{N}_2,0}$	0.997	0.995	0.987	0.953	0.942	0.927	0.850
$\alpha_{\mathcal{F}_1,0}$	1.073	1.089	1.196	1.513	1.515	1.557	1.619
$\alpha_{\mathcal{F}_2,0}$	1.016	1.022	1.049	1.168	1.166	1.182	1.172
$\alpha_{\mathcal{N}_1,5}$	0.995	0.992	0.984	0.948	0.937	0.921	0.848
$\alpha_{\mathcal{N}_2,5}$	0.997	0.995	0.989	0.959	0.948	0.933	0.858
$\alpha_{\mathcal{F}_1,5}$	1.026	1.035	1.075	1.195	1.224	1.247	1.248
$\alpha_{\mathcal{F}_2,5}$	1.010	1.014	1.031	1.094	1.109	1.119	1.097
$\alpha_{\mathcal{N}_1,8}$	0.997	0.996	0.990	0.961	0.951	0.937	0.863
$\alpha_{\mathcal{N}_2,8}$	0.998	0.997	0.992	0.965	0.956	0.942	0.868
$\alpha_{\mathcal{F}_1,8}$	1.010	1.014	1.087	1.116	1.101	1.111	1.087
$\alpha_{\mathcal{F}_2,8}$	1.006	1.008	1.051	1.051	1.059	1.063	1.028

Table 8: Fibrotic Lung - Scenario 1 - Mean apparent contrasts computed from the original emission and annihilation images for all studied radionuclides. $\mathcal{C}_{\cdot,i}$ is the apparent contrast between VOIs (description in 3.2), after a postfilter of FWHM i mm.

Measure	^{18}F	^{64}Cu	^{89}Zr	^{15}O	^{68}Ga	^{124}I	^{82}Rb
$\mathcal{C}_{\mathcal{F}_1/\mathcal{N}_1,0}$	1.073	1.103	1.195	1.511	1.581	1.645	1.862
$\mathcal{C}_{\mathcal{F}_2/\mathcal{N}_2,0}$	1.015	1.021	1.051	1.167	1.199	1.231	1.322
$\mathcal{C}_{\mathcal{F}_1/\mathcal{N}_1,5}$	1.028	1.039	1.082	1.232	1.272	1.312	1.419
$\mathcal{C}_{\mathcal{F}_2/\mathcal{N}_2,5}$	1.011	1.016	1.036	1.119	1.143	1.169	1.239
$\mathcal{C}_{\mathcal{F}_1/\mathcal{N}_1,8}$	1.011	1.016	1.083	1.116	1.139	1.163	1.230
$\mathcal{C}_{\mathcal{F}_2/\mathcal{N}_2,8}$	1.006	1.009	1.047	1.076	1.093	1.111	1.163

Table 9: Fibrotic Lung - Scenario 2 - Mean apparent recovery values computed from the original emission and annihilation images for all studied radionuclides. $\alpha_{\mathcal{V},i}$ is the apparent recovery for a VOI $\mathcal{V}$ (description in 3.2), after a postfilter of FWHM i mm.

Measure	^{18}F	^{64}Cu	^{89}Zr	^{15}O	^{68}Ga	^{124}I	^{82}Rb
$\alpha_{\mathcal{N}_1,0}$	1.003	1.001	1.006	1.014	1.002	1.009	0.975
$\alpha_{\mathcal{N}_2,0}$	1.000	1.000	1.001	1.005	1.002	1.000	0.966
$\alpha_{\mathcal{F}_1,0}$	1.011	1.004	1.009	1.006	1.000	0.993	0.956
$\alpha_{\mathcal{F}_2,0}$	1.001	0.999	0.999	0.995	0.991	0.987	0.939
$\alpha_{\mathcal{N}_1,5}$	1.001	1.001	1.002	1.007	1.002	1.001	0.968
$\alpha_{\mathcal{N}_2,5}$	1.000	1.000	1.001	1.003	1.001	0.999	0.964
$\alpha_{\mathcal{F}_1,5}$	1.001	1.000	0.999	0.995	0.989	0.984	0.938
$\alpha_{\mathcal{F}_2,5}$	1.000	0.999	0.999	0.995	0.991	0.986	0.936
$\alpha_{\mathcal{N}_1,8}$	1.000	1.000	1.001	1.003	1.000	0.999	0.963
$\alpha_{\mathcal{N}_2,8}$	1.000	1.000	1.001	1.001	1.000	0.998	0.959
$\alpha_{\mathcal{F}_1,8}$	1.000	0.999	0.999	0.993	0.988	0.982	0.932
$\alpha_{\mathcal{F}_2,8}$	1.000	1.000	0.999	0.994	0.990	0.984	0.932

5. Discussion

In this work, we have simulated in the lung two different scenarios. In the first scenario, the entire lung (comprising of healthy lung, lung tumour or fibrotic lung) was considered to have the same radioactivity concentration. In the second scenario, the air in the lung was assumed to contain no radioactivity, meaning the radioactivity was evenly distributed over the "tissue" in the lung (defined as "everything but the air"). The latter scenario corresponds to the situation where the normal lung tissue has the same radiotracer uptake as the tumour or fibrotic tissue.

The results of the simulations show that, although positron range is usually perceived as a blurring effect, in heterogeneous media it should rather be considered as a more complex change in the apparent radioactivity distribution, as high-density

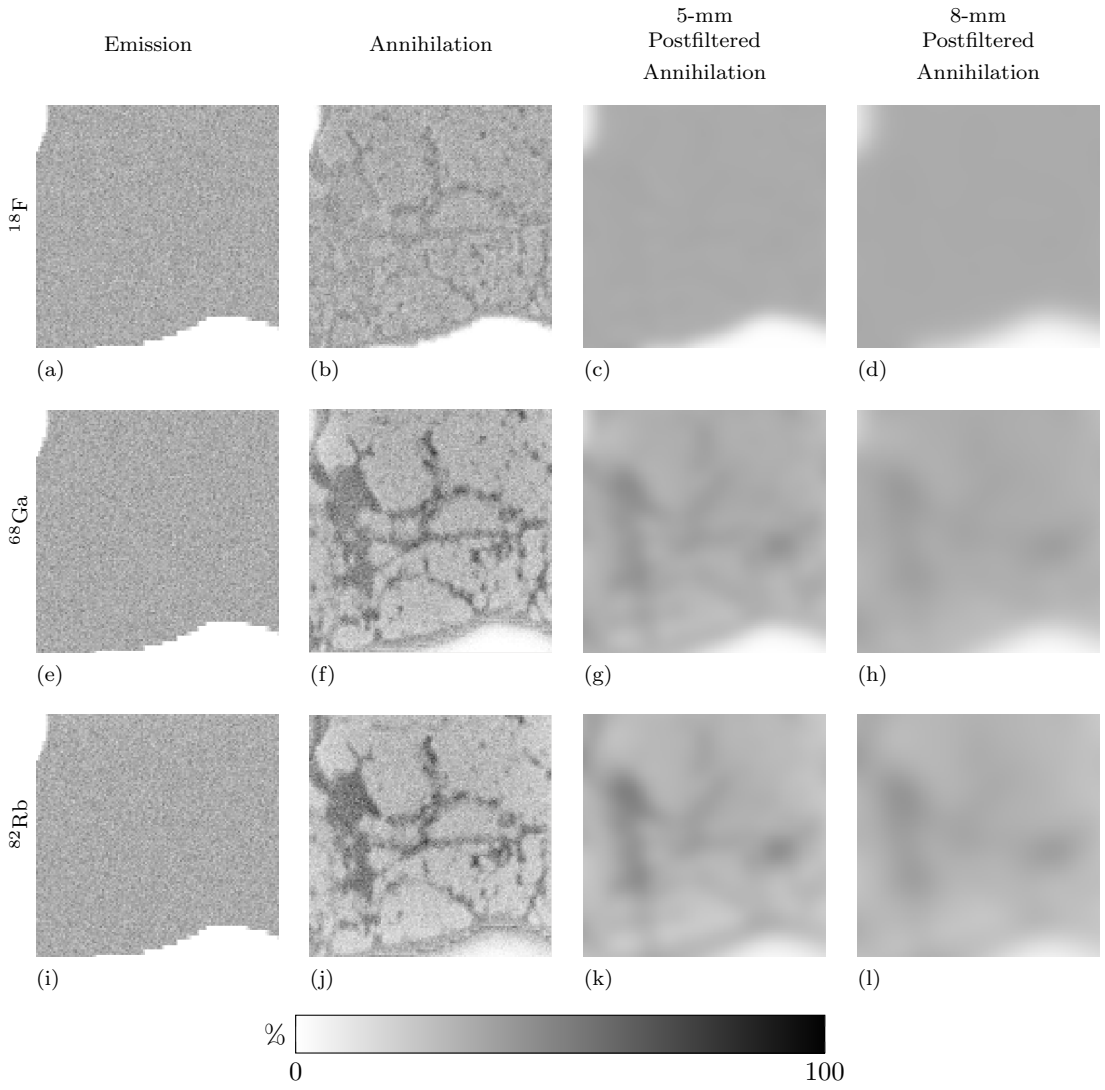

Figure 7: Fibrotic Lung - Scenario 1 - (a) (resp. (e), (i)) emission events, (b) (resp. (f), (j)) annihilation events, (c) (resp. (g), (k)) 5 mm postfiltered annihilation events and (d) (resp. (h), (l)) 8 mm postfiltered annihilation events computed for ^{18}F (top row) (resp. ^{68}Ga (middle row), ^{82}Rb (bottom row)). All images are scaled using the same colourbar (110% of the maximal value of the unfiltered ^{82}Rb annihilation image).

structures are more likely to "capture" some of the activity from the neighbouring lower density structures, than the opposite.

In the case of a high-density tumour located within a healthy lung, a part of the activity of the surrounding low-density area will be transferred to the tumour ("spill-in"), as well as some activity from the tumour to the healthy lung ("spill-out"). In the first scenario (even distribution), the tumour will appear hotter on the PET images, as the spill-out is largely dominated by the spill-in. However, in the second scenario (air containing no radioactivity), the spill-out now balances the spill-

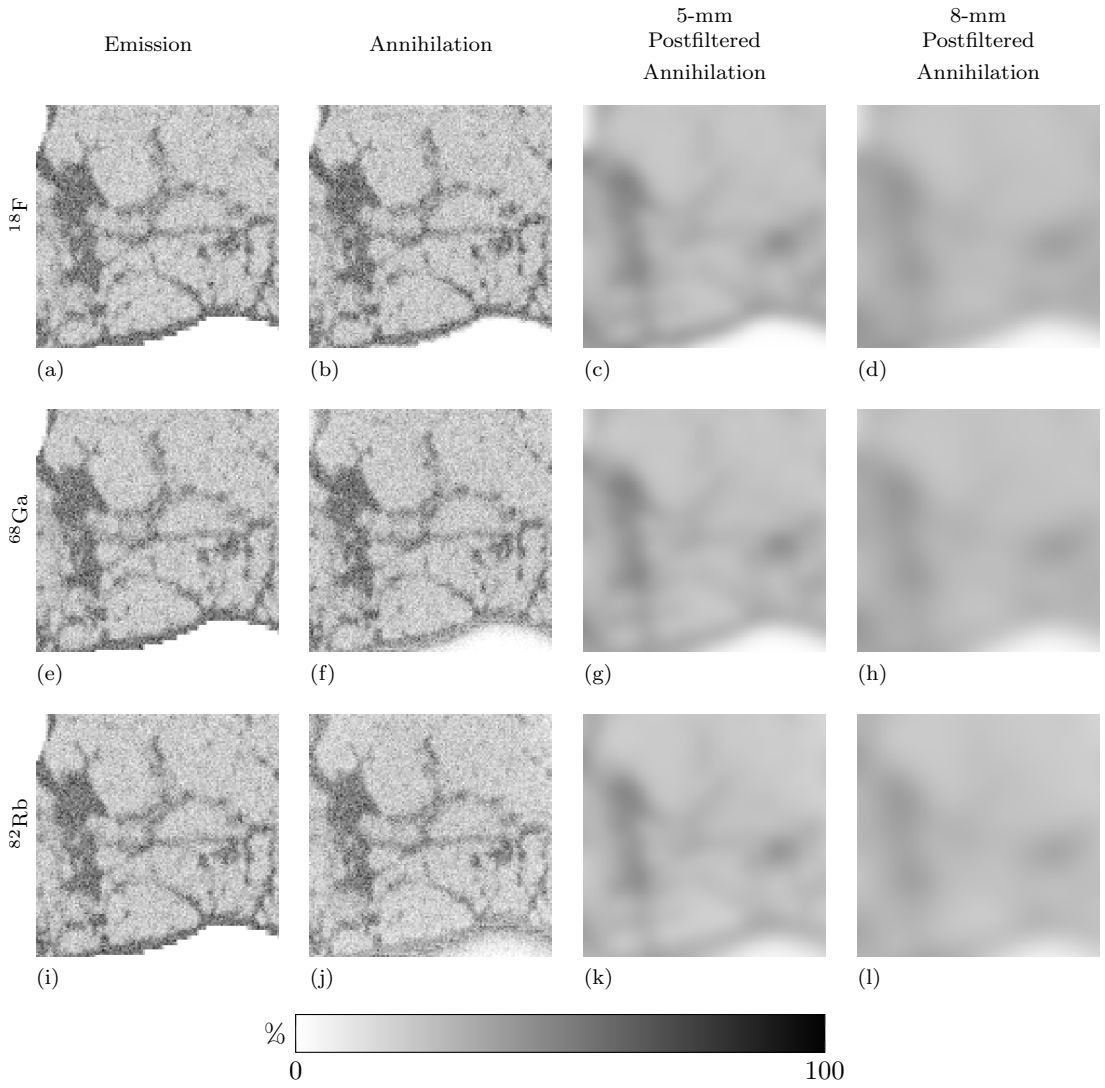

Figure 8: Fibrotic Lung - Scenario 2 - (a) (resp. (e), (i)) emission events, (b) (resp. (f), (j)) annihilation events, (c) (resp. (g), (k)) 5 mm postfiltered annihilation events and (d) (resp. (h), (l)) 8 mm postfiltered annihilation events computed for ^{18}F (top row) (resp. ^{68}Ga (middle row), ^{82}Rb (bottom row)). All images are scaled using the same colourbar (maximal value of the unfiltered ^{82}Rb annihilation image).

in, which leads to apparent recovery values ≈ 1. When varying the level of activity in the surrounding healthy lung (see Figure 6), the changes of spill-in and spill-out fractions lead to either positive or negative biases in the apparent recovery values. The radioactivity distribution of Scenario 2 acts as a "threshold": when the radioactivity of the healthy lung is lower than the one of Scenario 2, the recovery values will be negatively impacted, if higher, positively impacted. When there is no activity in the healthy lung, the observations are consistent with Kemerink et al. (2011), where a similar experiment was performed using syringes of various sizes containing activity in water

(water density ≈ lung tumour density). They were placed in cellular polyethylene foam (density $0.164\,\mathrm{g}\cdot\mathrm{cm}^{-3}$) to mimic a healthy lung. As no background activity was used (therefore observing only spill-out from the syringe), only spill-out was observed, which led to a negative bias in the tumour recovery values.

The spill-in effect of the positron range is mostly noticeable at the edges of the tumour, with the "penetration depth" depending on the radionuclide and expected to be related to the "mean positron range in water", with $R_{\mathrm{mean}} \approx 5\,\mathrm{mm}$ for ^{82}Rb, i.e. half the radius). That implies that the spill-in effects need to be considered for structures of about twice the mean positron range – the magnitude depending on the radioactive concentration in the background. In this study, lung tumours were modelled with a uniform density and a spherical shape. The composition of a lung tumour is usually more diverse (e.g. with necrotic regions, see Travis et al. (2015)) and could lead to more complex positron range effects.

The results from the simulation of a fibrotic lung show the same trend as for the tumour. In the first scenario (uniform distribution), a large bias in the apparent radioactivity of the fibrotic lung is observed (up to ≈ +61.9% for unfiltered ^{82}Rb images), with a highly heterogeneous distribution overall. In the second scenario (air containing no activity), the apparent recovery ratio is slightly less than 1 for high-energy radionuclides, meaning that the spill-out is now dominant (minimum found of 0.939 in a VOI of dimension $9\,\mathrm{x}\,9\,\mathrm{x}\,9\,\mathrm{mm}^3$ for ^{82}Rb).

The observations shown here have implications for other situations. For example, the shift in measured radionuclide concentration to the higher density medium could be observed in the case of a metal implant or prosthetic in close proximity to a low-density medium. Such effect could be expected for cardiac imaging near the lung, however the effect of cardiac motion might prevail. Also, Chronic Obstructive Pulmonary Disease, one of the main causes of global mortality (Martinez et al. 2011) is mainly characterised by emphysema and air trapping, which leads to a locally lower density of the lung, meaning that positron range effects may be more prominent for this pathology. More generally the spill-in dominance is most relevant for cold-spot imaging, such as the detection of myocardial defects in PET (Rahmim et al. 2008). However for most purposes, PET tracers are more likely to have higher uptake in high-density regions (as expected for ^{18}F-FDG in IPF (Win et al. 2012)). The second scenario is therefore more realistic and the increase of apparent recovery in the high-density regions due to spill-in from the background healthy regions should be limited in the case where spill-out dominates, e.g. in tumour imaging. Our aim in this study was to better understand the possible effects that may be introduced in lung studies due to positron range, with particular emphasis on the quantitative bias that may be introduced. Our simulations therefore were conducted without noise so that the source of bias could be easily visualised. In practice, when noise is present, the underlying distribution of annihilation locations may not be visually observed, however, bias in quantitative measurements would remain. We therefore consider that the noise-free illustrative examples are useful. The effect of positron range will also be more visible for pre-clinical

systems, because of better spatial resolution (Yang et al. 2016). Note that, positron ranges were found to be lower than ranges estimated with alternative models (Cal-González et al. 2010, Jødal et al. 2012, Jødal et al. 2014), suggesting that the positron range effect might be underestimated in this work. Nonetheless, the results of the simulations presented in this paper (without postfiltering) may provide an indication of the magnitude of this effect, although additional simulations with appropriate object size as well as phantom acquisitions would be necessary to assess this in detail.

This paper was aimed at providing some insights on the effect of positron range in heterogeneous media. The use within an iterative reconstruction of anisotropic kernels (Bai et al. 2003, Alessio & MacDonald 2008, Szirmay-Kalos et al. 2012, Rahmim et al. 2008, Cal-González et al. 2015) or Monte Carlo simulations (Lehnert et al. 2011) could be verified for positron range compensation: the effects and bias observed in this work could potentially be reduced by incorporating one of these strategies, however the high computational cost might be a limiting factor in clinical settings (especially for the fibrotic lung where no clear uniform region can be used for correction); this will be the subject of future work. In the absence of an accurate positron range compensation method, when measuring the radioactivity concentration of a tumour or localised high-density regions in the lung, the reported radioactivity concentration values should be evaluated with caution when using of a tracer labelled with a radionuclide that emits high-energy positrons.

6. Conclusion

Positron range can be an important source of image degradation in PET imaging, as the events recorded by the detectors are not directly reflecting the radioactivity, but the annihilation events that occur after the radioactive decay. The effect is often considered as a blurring due to spill-out. Whilst this the case in soft tissues and more generally in a region where the density is homogeneous, in heterogeneous media the actual effect observed in this paper is more complex, especially in the presence of boundaries between high and low density materials.

We have shown that in the lung, there is a bias in the annihilation images (in addition to the apparent blurring) as a result of the interface of the low-density healthy lung with small structures of high density, such as tumours or fibrosis. This bias is due to the fact that the probability of positron annihilation is higher in the high-density features, therefore resulting in positive bias in activity in the high-density regions and negative bias in the low-density regions. Our simulations indicate that this effect may be important for imaging radionuclides emitting high-energy positrons such as ^{68}Ga, ^{124}I or ^{82}Rb when both media have a similar radioactivity concentration. However, for low-energy positrons or for cases where the high-density medium has a higher radioactivity than low-density medium, e.g. due to a different fraction of air, the spill-out becomes more predominant and other types of image degradation (e.g. due to data acquisition and reconstruction inaccuracies) are expected to have a larger impact on the quantification.

Acknowledgments

The authors acknowledge funding support from GlaxoSmithKline (BIDS3000030921) and research support from the National Institute for Health Research, University College London Hospitals Biomedical Research Centre.

References

Agostinelli S, Allison J, Amako K, Apostolakis J & Araujo H 2003 GEANT4 – a simulation toolkit *Nuclear Instruments and Methods in Physics Research A* **506**, 250–303.

Alessio A & MacDonald L 2008 Spatially variant positron range modeling derived from ct for pet image reconstruction *IEEE Nuclear Science Symposium Conference Record*.

Bai B, Ruangma A, Laforest R, Tai Y C & Leahy R 2003 Positron range modeling for statistical PET image reconstruction *2003 IEEE Nuclear Science Symposium. Conference Record (IEEE Cat. No.03CH37515)* **4**(2), 2501–2505.

Bettinardi V, Presotto L, Rapisarda E, Picchio M, Gianolli L & Gilardi M C 2011 Physical Performance of the new hybrid PETCT Discovery-690 *Medical Physics* **38**(10), 5394.

Blanco A 2006 Positron range effects on the spatial resolution of rpc-pet *IEEE Nuclear Science Symposium Conference Record*.

Brookhaven National Laboratory 2019 'National nuclear data center' `http://www.nndc.bnl.gov`. Accessed: 2019-05-21.

Cal-González J, Pérez-Liva M, Herraiz J L, Vaquero J J, Desco M & Udías J M 2015 Tissue-Dependent and Spatially-Variant Positron Range Correction in 3D PET *IEEE Transactions on Medical Imaging* **34**(11), 2394–2403.

Cal-González J et al. 2010 Validation of penelopet positron range estimations *IEEE Nuclear Science Symposium Conference Record*.

Cal-González J et al. 2013 Positron range estimations with penelopet *Physics in Medicine and Biology* **58**(15), 156–161.

Chang S et al. 1999 Five different anti-prostate-specific membrane antigen (psma) antibodies confirm psma expression in tumor-associated neovasculature *Cancer Research* **59**(13), 3192–3198.

Chen D, Cheriyan J, Chilvers E et al. 2017 Quantification of lung pet images: Challenges and opportunities *Journal of Nuclear Medicine* **58**(2), 201–207.

Derenzo S 1979 Precision measurement of annihilation point spread distributions for medically important positron emitters *International Conference on Positron Annihilation*.

Evans R 1955 *The Atomic Nucleus* Krieger Publishing Company.

Jakoby B W, Bercier Y, Conti M, Casey M E, Bendriem B & Townsend D W 2011 Physical and clinical performance of the mCT time-of-flight PET/CT scanner *Physics in Medicine and Biology* **56**(8), 2375–2389.

Jan S, Santin G, Strul D, Staelens S, Assié K, Autret D, Avner S, Barbier R, Bardiès M, Bloomfield P M, Brasse D, Breton V, Bruyndonckx P, Buvat I, Chatziioannou A F, Choi Y, Chung Y H, Comtat C, Donnarieix D, Ferrer L, Glick S J, Groiselle C J, Guez D, Honore P F, Kerhoas-Cavata S, Kirov A S, Kohli V, Koole M, Krieguer M, van der Laan D J, Lamare F, Largeron G, Lartizien C, Lazaro D, Maas M C, Maigne L, Mayet F, Melot F, Merheb C, Pennacchio E, Perez J, Pietrzyk U, Rannou F R, Rey M, Schaart D R, Schmidtlein C R, Simon L, Song T Y, Vieira J M, Visvikis D, Van De Walle R, Wieërs E & Morel C 2004 GATE - Geant4 Application for Tomographic Emission: a simulation toolkit for PET and SPECT *Physics in Medicine & Biology* **49**(19), 4543–4561.

Jødal L, Le Loirec C & Champion C 2014 Positron range in PET imaging : non-conventional isotopes *Phys. Med. Biol* **59**(1), 7419–7434.

Jødal L et al. 2012 Positron range in pet imaging: an alternative approach for assessing and correcting the blurring *Phys. Med. Biol.* **57**(12), 3931–3943.

Kemerink G J, Visser M G W, Franssen R, Beijer E, Zamburlini M, Halders S G E A, Brans B, Mottaghy F M & Teule G J J 2011 Effect of the positron range of 18F, 68Ga and 124I on PET/CT in lung-equivalent materials *European Journal of Nuclear Medicine and Molecular Imaging* **38**(5), 940–948.

Kolthammer J A, Su K h, Grover A, Narayanan M, Muzic R F & Healthcare P 2015 Performance evaluation of the Ingenuity TF PET/CT scanner with a focus on high count-rate conditions **59**(14), 3843–3859.

Laboratoire National Henri Becquerel 2018 'Tables of recommended radionuclide data' `http://www.lnhb.fr/nuclear-data/`. Accessed: 2019-01-15.

Lambrou T, Groves A M, Erlandsson K, Screaton N, Endozo R, Win T, Porter J C & Hutton B F 2011 The importance of correction for tissue fraction effects in lung PET: Preliminary findings *European Journal of Nuclear Medicine and Molecular Imaging* **38**(12), 2238–2246.

Lehnert W et al. 2011 Analytical positron range modelling in heterogeneous media for pet monte carlo simulation *Phys. Med. Biol.* **56**(11), 3313–3335.

Levin C & Hoffman E 1970 Calculation of positron range and its effect on the fundamental limit of positron emission tomography system spatial resolution *Physical in Medicine and Biology* **44**(1).

Martinez F et al. 2011 The future of chronic obstructive pulmonary disease treatment - difficulties of and barriers to drug development *The Lancet* **378**, 1027–1037.

Moses W W 2011 Fundamental Limits of Spatial Resolution in PET William *Nuclear Inst. and Methods in Physics Research, A* **648**(Supplement 1), S236–S240.

Nakamura H, Saji H, Marushima H & Kimura H 2015 Standardized Uptake Values in the Primary Lesions of Non-Small- Cell Lung Cancer in FDG-PET / CT Can Predict Regional Lymph Node Metastases pp. 1388–1393.

Postmus P E, Kerr K M, Oudkerk M, Senan S, Waller D A, Vansteenkiste J, Escriu C, Peters S & on behalf of the ESMO Guidelines Committee 2017 Early and locally advanced non-small-cell lung cancer (nsclc): Esmo clinical practice guidelines for diagnosis, treatment and follow-up *Annals of Oncology* **28**(4), 1–21.

Rahmim A, Tang J, Lodge M A, Lashkari S, Mohammad R A & Bengel F M 2008 Resolution modeled PET image reconstruction incorporating space-variance of positron range: Rubidium-82 cardiac PET imaging *IEEE Nuclear Science Symposium Conference Record* pp. 3643–3650.

Reichert J M & Valge-Archer V E 2007 Development trends for monoclonal antibody cancer therapeutics. *Nat. Rev. Drug Discov.* **6**(5), 349–56.

Spagnolo P et al. 2015 Idiopathic pulmonary fibrosis: An update *Annals of Medicine* **47**(1), 15–27.

Szirmay-Kalos L et al. 2012 Fast positron range calculation in heterogeneous media for 3d pet reconstruction *IEEE Nuclear Science Symposium Conference Record*.

Travis W D, Brambilla E, Nicholson A G, Yatabe Y, Austin J H, Beasley M B, Chirieac L R, Dacic S, Duhig E, Flieder D B, Geisinger K, Hirsch F R, Ishikawa Y, Kerr K M, Noguchi M, Pelosi G, Powell C A, Tsao M S & Wistuba I 2015 The 2015 World Health Organization Classification of Lung Tumors: Impact of Genetic, Clinical and Radiologic Advances since the 2004 Classification *Journal of Thoracic Oncology* **10**(9), 1243–1260.

Wang H et al. 2015 Expression of prostate-specific membrane antigen in lung cancer cells and tumor neovasculature endothelial cells and its clinical significance. *PloS one* **10**(5), 1–8.

Win T, Lambrou T, Hutton B F, Kayani I, Screaton N J, Porter J C, Maher T M, Endozo R, Shortman R I, Lukey P & Groves A M 2012 18F-Fluorodeoxyglucose positron emission tomography pulmonary imaging in idiopathic pulmonary fibrosis is reproducible: Implications for future clinical trials *European Journal of Nuclear Medicine and Molecular Imaging* **39**(3), 521–528.

Wolfram Research I 2017 'Mathematica, Version 11.2'.

Xu D M, van Klaveren R J, de Bock G H, Leusveld A, Zhao Y, Wang Y, Vliegenthart R, de Koning H J, Scholten E T, Verschakelen J, Prokop M & Oudkerk M 2008 Limited value of shape, margin and

CT density in the discrimination between benign and malignant screen detected solid pulmonary nodules of the NELSON trial *European Journal of Radiology* **68**(2), 347–352.

Yang Y, Bec J, Zhou J, Zhang M, Judenhofer M S, Bai X, Di K, Wu Y, Rodriguez M, Dokhale P, Shah K S, Farrell R, Qi J & Cherry S R 2016 A Prototype High-Resolution Small-Animal PET Scanner Dedicated to Mouse Brain Imaging *Journal of Nuclear Medicine* **57**(7), 1130–1135.

Appendix A. Lung Tumour Material in GATE

```
LungTumour:   d=1.028 g/cm3 ; n=8
        +el: name=Hydrogen    ; f=0.106
        +el: name=Carbon      ; f=0.284
        +el: name=Nitrogen    ; f=0.026
        +el: name=Oxygen      ; f=0.578
        +el: name=Phosphor    ; f=0.001
        +el: name=Sulfur      ; f=0.002
        +el: name=Chlorine    ; f=0.002
        +el: name=Potassium   ; f=0.001
```

Appendix B. Fibrotic Lung Materials in GATE

```
LungTissue:   d=0.89 g/cm3 ; n=9
        +el: name=Hydrogen   ; f=0.106
        +el: name=Carbon     ; f=0.096
        +el: name=Nitrogen   ; f=0.019
        +el: name=Oxygen     ; f=0.765
        +el: name=Sodium     ; f=0.003
        +el: name=Phosphor   ; f=0.003
        +el: name=Sulfur     ; f=0.004
        +el: name=Chlorine   ; f=0.003
        +el: name=Potassium  ; f=0.001
```

```
Lung-800:    d=0.26 g/cm3 ; n=3
        +mat: name=Air                  ; f=0.74
        +mat: name=Blood                ; f=0.16
        +mat: name=LungTissue           ; f=0.1
Lung-750:    d=0.289 g/cm3 ; n=3
        +mat: name=Air                  ; f=0.7067
        +mat: name=Blood                ; f=0.16
        +mat: name=LungTissue           ; f=0.1333
Lung-700:    d=0.319 g/cm3 ; n=3
        +mat: name=Air                  ; f=0.6734
        +mat: name=Blood                ; f=0.16
        +mat: name=LungTissue           ; f=0.1666
Lung-650:    d=0.348 g/cm3 ; n=3
        +mat: name=Air                  ; f=0.6401
        +mat: name=Blood                ; f=0.16
        +mat: name=LungTissue           ; f=0.1999
Lung-600:    d=0.378 g/cm3 ; n=3
        +mat: name=Air                  ; f=0.6068
```

```
        +mat: name=Blood                ; f=0.16
        +mat: name=LungTissue           ; f=0.2332
Lung-550:   d=0.408 g/cm3 ; n=3
        +mat: name=Air                  ; f=0.5735
        +mat: name=Blood                ; f=0.16
        +mat: name=LungTissue           ; f=0.2665
Lung-500:   d=0.437 g/cm3 ; n=3
        +mat: name=Air                  ; f=0.5402
        +mat: name=Blood                ; f=0.16
        +mat: name=LungTissue           ; f=0.2998
Lung-450:   d=0.467 g/cm3 ; n=3
        +mat: name=Air                  ; f=0.5069
        +mat: name=Blood                ; f=0.16
        +mat: name=LungTissue           ; f=0.3331
Lung-400:   d=0.496 g/cm3 ; n=3
        +mat: name=Air                  ; f=0.4736
        +mat: name=Blood                ; f=0.16
        +mat: name=LungTissue           ; f=0.3664
Lung-350:   d=0.526 g/cm3 ; n=3
        +mat: name=Air                  ; f=0.4403
        +mat: name=Blood                ; f=0.16
        +mat: name=LungTissue           ; f=0.3997
Lung-300:   d=0.555 g/cm3 ; n=3
        +mat: name=Air                  ; f=0.407
        +mat: name=Blood                ; f=0.16
        +mat: name=LungTissue           ; f=0.433
Lung-250:   d=0.585 g/cm3 ; n=3
        +mat: name=Air                  ; f=0.3737
        +mat: name=Blood                ; f=0.16
        +mat: name=LungTissue           ; f=0.4663
Lung-200:   d=0.615 g/cm3 ; n=3
        +mat: name=Air                  ; f=0.34
        +mat: name=Blood                ; f=0.16
        +mat: name=LungTissue           ; f=0.5
```